

# An efficient numerical model for incompressible two-phase flow in fractured media

Hussein Hoteit<sup>a,1</sup>, Abbas Firoozabadi<sup>a,b,\*</sup>

<sup>a</sup> Reservoir Engineering Research Institute, Palo Alto, CA, USA

<sup>b</sup> Yale University, New Haven, CT, USA

## ARTICLE INFO

### Article history:

Received 1 October 2007

Received in revised form 1 February 2008

Accepted 19 February 2008

Available online 7 March 2008

### Keywords:

Two-phase flow

Water injection

Fractured media

Heterogeneous media

Capillary pressure

Discrete fractured model

Mixed finite element method

Discontinuous Galerkin

IMPES methods

## ABSTRACT

Various numerical methods have been used in the literature to simulate single and multiphase flow in fractured media. A promising approach is the use of the discrete-fracture model where the fracture entities in the permeable media are described explicitly in the computational grid. In this work, we present a critical review of the main conventional methods for multiphase flow in fractured media including the finite difference (FD), finite volume (FV), and finite element (FE) methods, that are coupled with the discrete-fracture model. All the conventional methods have inherent limitations in accuracy and applications. The FD method, for example, is restricted to horizontal and vertical fractures. The accuracy of the vertex-centered FV method depends on the size of the matrix gridcells next to the fractures; for an acceptable accuracy the matrix gridcells next to the fractures should be small. The FE method cannot describe properly the saturation discontinuity at the matrix–fracture interface. In this work, we introduce a new approach that is free from the limitations of the conventional methods. Our proposed approach is applicable in 2D and 3D unstructured gridings with low mesh orientation effect; it captures the saturation discontinuity from the contrast in capillary pressure between the rock matrix and fractures. The matrix–fracture and fracture–fracture fluxes are calculated based on powerful features of the mixed finite element (MFE) method which provides, in addition to the gridcell pressures, the pressures at the gridcell interfaces and can readily model the pressure discontinuities at impermeable faults in a simple way. To reduce the numerical dispersion, we use the discontinuous Galerkin (DG) method to approximate the saturation equation. We take advantage of a hybrid time scheme to alleviate the restrictions on the size of the time step in the fracture network. Several numerical examples in 2D and 3D demonstrate the robustness of the proposed model. Results show the significance of capillary pressure and orders of magnitude increase in computational speed compared to previous works.

© 2008 Elsevier Ltd. All rights reserved.

## 1. Introduction

Modeling of multiphase fluid flow in fractured media is of interest in many of the environmental and energy problems. Examples include tracing a NAPL migration, radioactive waste management in the subsurface, and the enhanced oil recovery in naturally fractured reservoirs. Geological characterization and multiphase flow simulation are challenging tasks in complex fractured media. Various conceptual models have been used to describe multiphase flow in fractured media. The main models include the dual-porosity and its variations, single-porosity, and the discrete-fractured approaches.

The dual-porosity model has traditionally been used to simulate the flow in fractured hydrocarbon reservoirs [1–6]. In this model, the matrix–fracture mass transfer is described by empirical func-

tions that incorporate ad hoc shape factors which are based on theoretical derivations in single phase. In two-phase with capillary and gravity, there is no theory for the calculation of shape factors despite the fact that the accuracy of flow calculations depend on their values. The problem may be even more fundamental. The driving force in the expression of the transfer function in two-phase flow may not have a sound basis. We should point out that advanced variations of the dual-porosity model such as the multiple interaction continua method [7] have better accuracy and features than the conventional model.

A more accurate and physics-based approach is the single-porosity model that describes fractures explicitly in the medium. This model requires the fracture-network characterization and the fracture–fluid interaction functions. Modeling fractures with the single-porosity model can be classified as a complex case of heterogeneous porous media, where the fracture gridcells are treated similarly to the matrix gridcells. The implementation of this model is, however, almost impossible in field-scale problems because of excessive fine gridding and severe restrictions on the time steps due to the contrast in geometrical scales between the

\* Corresponding author. Address: Reservoir Engineering Research Institute, Palo Alto, CA, USA.

E-mail address: [af@rerinst.org](mailto:af@rerinst.org) (A. Firoozabadi).

<sup>1</sup> Now at ConocoPhillips Co.

fracture and the adjacent rock-matrix gridcells [8]. The matrix inversion due to ill-conditioning becomes a challenge.

The discrete-fracture model [9,10] describes the fractures explicitly in the medium similarly to the single-porosity model. However, unlike the single-porosity model, the fractures gridcells are geometrically simplified by using  $(n - 1)$ -dimensional gridcells in an  $n$ -dimensional domain. In other words, in 3D space, the fractures are represented by the matrix gridcell interfaces, which are 2D. This simplification removes the length-scale contrast caused by the explicit representation of the fracture aperture as in the single-porosity model. As a result, computational efficiency is improved considerably. However, the discrete-fracture model can only handle a limited number of fractures (of the order of thousands) for reasons related to computational resources. One approach to overcome this limitation is to model explicitly only the major fractures and use an upscaling technique to mimic the effect of the minor fractures [11].

Various numerical methods based on the discrete-fracture model have been used to simulate single and multiphase flow in fractured media. Methods that are developed for single-phase flow may not be trivially extended to two-phase flow. In two-phase flow, high permeable fractures may not be the main flow conduits due to the contrast in capillary pressure between the fracture and the rock matrix. Capillary pressure heterogeneity may also cause fluid trapping (discontinuous saturation) and, in some cases, pressure discontinuously [12–15]. The fluid streamlines may, therefore, change significantly with time. The discrete-fracture model has been used in the finite difference (FD), finite volume (FV), and the Galerkin finite element (FE). These methods may have some inherent limitations, as discussed below.

Slough et al. [16,17] used the FD method to simulate the migration of a NAPL in 2D and 3D fractured media in structured grids. They used distinct degrees of freedom for the saturation and pressure in the fracture and matrix control-volumes. In Cartesian gridding, the intersection of horizontal and vertical fractures corresponds to a control-volume that has the dimensions of the fracture thicknesses (see Fig. 1a). Such a control-volume may reduce significantly the size of the time step in the numerical model. To eliminate the degrees of freedom at the fracture junctions, Slough et al. used a technique based on steady-state flow equa-

tions. They suggested to use two-point upstream weighting to approximate the mobilities. The extension of their technique to a fracture gridcell that has several feeding fractures was not discussed. When the control-volume at the fractures junction in Fig. 1a is eliminated, one fracture gridcell may have up to three upstream fractures. Lee et al. [11] used a hierarchical approach based on fracture lengths such that “short” fractures are treated implicitly by increasing the effective matrix permeability while “long” fractures are described explicitly. Similarly to the model by Slough et al., the fractures were aligned with the matrix gridcells; that is, either vertical or horizontal. They used a technique for well productivity indices for single-phase flow (capillary pressure was neglected) to calculate the transmissibilities between the fracture and the matrix gridcells.

The Galerkin FE method has been used to model single-phase [9,10,18–20] and two-phase flow [21–23] in fractured media. In 2D space, the fractures are represented by 1D entities and the degrees of freedom are located at the mesh nodes (see Fig. 1b). The fractures and the adjacent matrix gridcells share the same degrees of freedom, therefore, there is an implicit assumption of the continuity of pressure and saturation at the matrix–fracture interface. As a result, the FE suffers from a weakness in two-phase flow because it cannot account properly for saturation discontinuity from capillary pressure contrast at the matrix–fracture interface.

Two FV methods with different spatial discretizations have been used for fractured media: (1) the cell-centered FV, and (2) the vertex-centered FV, which is also known as the control-volume finite element (CVFE) method. In the cell-centered FV, similarly to the FD (Fig. 1a), the fracture gridcells are located at the boundaries of the matrix gridcells. This approach can describe heterogeneities within the mesh, however, there is numerical complexity in defining the matrix–fracture and the fracture–fracture fluxes. Karimi-Fard et al. [24] introduced a simplified cell-centered FV method for two-phase flow in fractured media. The authors, however, mentioned that their method could create numerical errors in non-orthogonal grids because the fluxes are calculated by the two-point flux approximation method. They used an analogy between the conductance through resistors and flow in porous media to eliminate the control-volumes at fracture intersections, where capillary pressure and gravity effects are neglected. Grant et al. [25] also used the cell-centered FV method to model two-phase flow in 2D fractured media. To calculate the fracture–fracture flux, they introduced special nodes at the fracture intersections where they calculated the saturation at an intermediate time step.

Many authors have used the CVFE method and some have combined it with the Galerkin FE method to solve the two-phase flow equations in fractured media [26–31]. In the CVFE method, the fracture entities are embedded within the matrix control-volume (see Fig. 1c). In this approach, the calculation of the matrix–fracture flux is avoided and there is no difficulty in computing the fracture–fracture flux. However, consistent modeling of the saturation discontinuity from the capillary pressure contrast at the fracture–matrix interface has not been fully examined. Monteagudo and Firoozabadi [32] used the capillary pressure continuity equation at the matrix–fracture interface and the capillary pressure–saturation functions to calculate the saturations in the fracture and the matrix blocks within the same control-volume. In other words, the saturation within a control-volume is distributed between the matrix and fracture blocks so that the capillary-pressure continuity is preserved at the interface. This approach may become inefficient when the fracture capillary pressure is zero. Reichenberger et al. [33] used discontinuous approximation functions for the saturation in the fractures to account for the saturation discontinuity at the matrix–fracture interface. Similarly to the method of Monteagudo and Firoozabadi [32], this approach suffers from zero capillary pressure in the fracture.

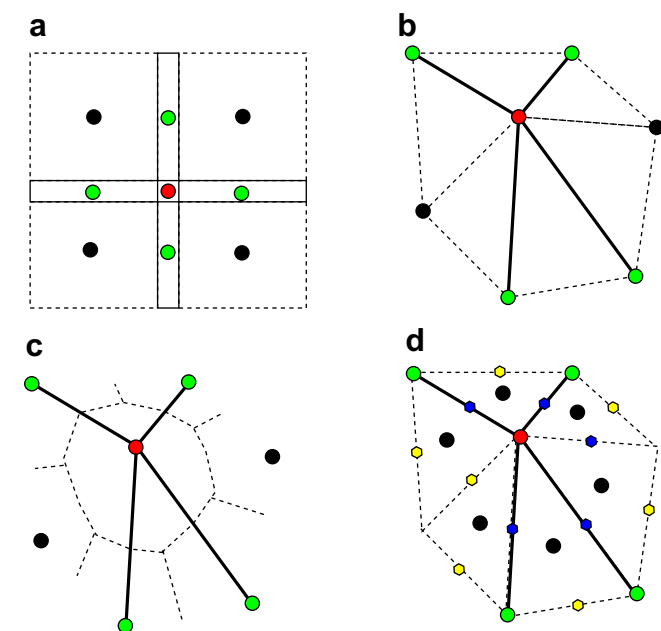


Fig. 1. Different spatial discretizations of the fractures and the adjacent matrix gridcells in FD, FE, CVFE, and MFE. (a) FD; (b) FE; (c) CVFE; (d) MFE.

There is another concern related to the matrix gridding that may affect the accuracy of the CVFE method in which one invokes a cross-flow equilibrium between the fracture and the adjacent matrix blocks. Here, the pressure in the fracture and that in the matrix are assumed equal within the same control-volume. In the CVFE approaches that ignore the capillary pressure heterogeneity, the same saturation is assumed within the control-volume. These assumptions are justifiable if the matrix gridcells next to the fractures are small enough. For an acceptable accuracy for an enhanced oil recovery problem (gas injection), Hoteit and Firoozabadi [34] found that the matrix-gridcells size next to the fractures should be of the order of ten centimeters in a fractured reservoir of length-scale in kilometers. Reichenberger et al. [33] also used very fine gridgings in their numerical experiments.

The mixed finite element (MFE) method [35,36] has received much attention for its powerful features in approximating the velocity field in highly heterogeneous and anisotropic media and has been widely used to model single-phase flow in fractured media. In Refs. [37,38], the method is used to simulate steady-state single-phase flow in fracture-networks and the mass transfer between the fractures and the rock matrix was neglected. Alboin et al. [39] employed the MFE to solve the transport equation in fractured media. Martin et al. [40] extended the work of Alboin et al. to model the cases when the fracture is less permeable than the matrix.

In this work, we extend the MFE method to two-phase flow in fractured media with gravity and capillarity and account for matrix–fracture interactions. In our algorithm, the use of the hybridized MFE method [41,36] overcomes the limitations of the numerical models discussed earlier. In our work, the degrees of freedom for the saturation and pressure in a fracture gridcell are not the same as those in the neighboring matrix gridcells (see Fig. 1d). As a result, one can describe readily the discontinuity in saturation from capillary pressure heterogeneity. The fractional flow (global pressure) formulation [42] in the MFE does not allow proper modeling of saturation discontinuity. We use instead a consistent formulation from Ref. [43] in which phase pressure serves as the primary unknown.

Most of the conventional approaches in the literature use two-point upstream weighting to approximate the mobilities. For some applications, this technique is known to provide poor accuracy [44,45]. In this work, we use the discontinuous Galerkin (DG) method [42,46,47] stabilized by a multidimensional slope limiter introduced by Chavent and Jaffré [42] to reduce the numerical dispersion in the saturation. The two-phase immiscible flow equations are solved by an implicit-pressure–explicit-saturation (IMPES) approach. The IMPES method may perform more efficiently than the fully-implicit method [48]. Its stability is, however, restricted to a CFL condition, which is inversely proportional to the gridcell pore-volumes. Therefore, the fracture gridcells may impose a severe CFL condition. To allow for high computational efficiency, we implement an implicit scheme in the fracture network and an explicit scheme in the matrix.

With above literature review on two-phase flow in fractured media, we are now set to first present the essence of the proposed model and to discuss the governing equations for two-phase immiscible flow in porous media. We then rewrite the flow equations in an equivalent form which is appropriate for the MFE formulation. The MFE formulations in the matrix and fracture domains are then applied to approximate the volumetric flux and the wetting-phase potential, where the capillary pressure is taken into account. This is followed by a description of the DG formulation and the proposed time scheme. Several examples in 2D and 3D are presented to show the applicability of our method.

In Ref. [43], we presented the formulation and the numerical method for two-phase flow in unfractured media. We focused on

modeling capillary pressure continuity/discontinuity and verified the accuracy of our method with analytical solutions in heterogeneous media. Some details presented in that work are not repeated in this paper.

## 2. Proposed method

In the conventional methods, the flux through gridcell interfaces is calculated in a post-processing step from the pressure field. In the MFE method, the flux and the pressure unknowns are approximated simultaneously. The original MFE method with the lowest order Raviart–Thomas space [35,49] leads to a saddle point problem, where the linear system to solve is indefinite. The hybridized MFE method [36,41] overcomes this problem by adding new degrees of freedom (Lagrange multipliers) that represent the pressure averages (traces of the pressure) on the gridcell interfaces. The original MFE and the hybridized MFE are algebraically equivalent [41,50]. The difference is only in the selection of the primary variables. In this work, we use the hybridized MFE, and for the sake of brevity we denote it also by MFE. Its primary variables are the traces of pressure; the secondary variables are the gridcell average pressures and the averages fluxes across the gridcell interfaces (see Fig. 2).

In our work, we assume capillary pressure continuity (that is, pressure continuity) at the matrix–fracture interface, except when the pressure of the non-wetting phase entering a different medium saturated with the wetting-phase is less than the threshold (entry) pressure [13–15]. The non-wetting phase becomes immobile and, therefore, there may be discontinuity in the non-wetting phase pressure. Modeling this phenomenon in heterogeneous media by the MFE method is discussed in Ref. [43]. For the sake of clarity, the discontinuity in capillary pressure is not discussed further in this work; we assume that the wetting phase is always displacing the non-wetting phase (imbibition) and so the pressures are always continuous.

In a previous work [51,52], we used the MFE method to simulate single and two-phase compositional flow in 2D fractured media but with neglected capillary pressure. We also invoked cross-flow equilibrium between the fracture and the adjacent matrix gridcells in a similar fashion as the CVFE method. In other words, the fracture pressure and the adjacent matrix gridcells pressures are assumed equal (see Fig. 2). As discussed in Section 1, this simplification is justifiable if the matrix gridcells next to the fracture are small.

A central idea in our work is a new formulation that does not invoke the cross-flow equilibrium across the fractures and the neighboring matrix blocks. We assume a constant potential along the width of the fracture gridcells (see Fig. 3) and therefore cross-flow equilibrium is assumed across the fractures only. As sketched in Fig. 3, the degrees of freedom for the potential and sat-

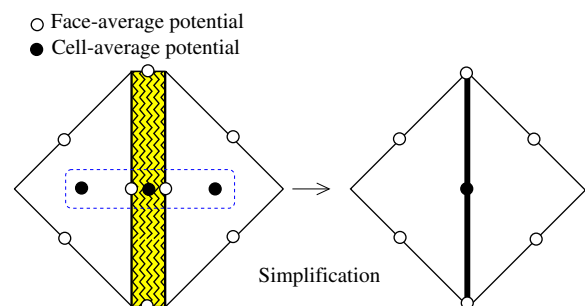


Fig. 2. Modeling of flow in fractured media using the cross-flow equilibrium in the fractures and the adjacent matrix gridcells.

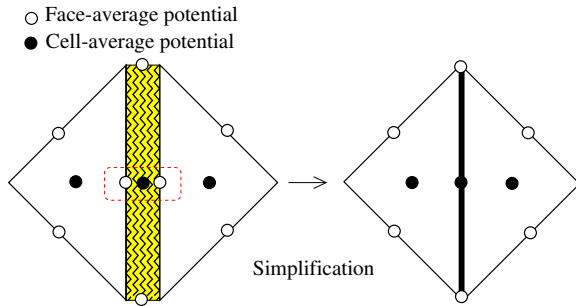


Fig. 3. Modeling of flow in fractured media using our proposal without the cross-flow equilibrium.

uration in the matrix and fracture gridcells are distinct. This new approach alleviates the size constraint on the matrix gridcells next to the fractures and allows accurate calculation of the saturations in the fracture and in the adjacent matrix gridcells without a need for small neighboring matrix blocks. Our proposal has similarities to the conventional single-porosity model, however there is a significant advantage as it allows accurate and efficient calculation of the matrix–fracture and fracture–fracture flux, as will be discussed later.

### 3. Governing equations

The governing equations in porous media for the flow of two incompressible and immiscible phases, a wetting phase (referred to by the subscript  $w$ ), and a non-wetting phase (referred to by the subscript  $n$ ), are given by the saturation equation and the generalized Darcy law of each phase. Saturation constraint and the capillary pressure relation complete the formulation:

$$\phi \frac{\partial S_\alpha}{\partial t} + \nabla \cdot (\mathbf{v}_\alpha) = F_\alpha, \quad \alpha = n, w, \quad (1)$$

$$\mathbf{v}_\alpha = -\frac{k_{r\alpha}}{\mu_\alpha} \mathbf{K} (\nabla p_\alpha + \rho_\alpha g \nabla z), \quad \alpha = n, w, \quad (2)$$

$$S_n + S_w = 1, \quad (3)$$

$$p_c(S_w) = p_n - p_w. \quad (4)$$

In the above equations,  $\mathbf{K}$  is the absolute permeability tensor,  $S_\alpha$ ,  $p_\alpha$ ,  $\rho_\alpha$ ,  $k_{r\alpha}$ ,  $F_\alpha$ , and  $\mu_\alpha$  are the saturation, pressure, density, relative permeability, sink/source term, and viscosity of phase  $\alpha$ , respectively,  $g$  is the gravity acceleration,  $z$  is the depth, and  $p_c$  is the capillary pressure.

As discussed in Ref. [43], the MFE method was initially proposed for single-phase flow in porous media. A number of authors have used the fractional flow formulation (also known as the global pressure formulation) to extend the MFE for two-phase flow. The MFE method with the fractional flow formulation, however, becomes inconsistent for the simulation of flow in heterogeneous media with different capillary functions. A consistent formulation, that overcomes the fractional flow deficiency, is provided in Ref. [43]. A brief review of the formulation follows.

We define the flow potential,  $\Phi_\alpha$ , of phase  $\alpha$  as follows:

$$\Phi_\alpha = p_\alpha + \rho_\alpha g z, \quad \alpha = n, w. \quad (5)$$

The capillary potential,  $\Phi_c$ , becomes:

$$\Phi_c = \Phi_n - \Phi_w = p_c + (\rho_n - \rho_w) g z. \quad (6)$$

Then, Eqs. (1) and (2) are rewritten in the following equivalent forms:

$$\nabla \cdot (\mathbf{v}_a + \mathbf{v}_c) = F_t, \quad (7)$$

$$\phi \frac{\partial S_w}{\partial t} + \nabla \cdot (f_w \mathbf{v}_a) = F_w, \quad (8)$$

where the velocity variables  $\mathbf{v}_a$  and  $\mathbf{v}_c$ , whose sum is the total velocity, are given by:

$$\mathbf{v}_a = -\lambda_t \mathbf{K} \nabla \Phi_w, \quad (9)$$

$$\mathbf{v}_c = -\lambda_n \mathbf{K} \nabla \Phi_c. \quad (10)$$

In the above equations,  $\lambda_\alpha = k_{r\alpha}/\mu_\alpha$  is the mobility of phase  $\alpha$ ,  $\lambda_t = \lambda_n + \lambda_w$  is the total mobility,  $f_w = \lambda_w/\lambda_t$  is the wetting-phase fractional function, and  $F_t = F_n + F_w$  is the total sink/source term.

The system of Eqs. (7) and (8) are subject to Neumann (flow rate control) and Dirichlet (pressure control) boundary conditions. The system of Eqs. (7)–(10) and the initial and boundary conditions are our working equations with the MFE and DG methods.

### 4. Approximation of the volumetric flux

The pressure and the saturation equations are decoupled and solved sequentially in an IMPES-like approach. However, we suggest the use of a different temporal scheme for the saturation equation in the fractures, as will be discussed later. The MFE method is used to approximate implicitly the pressure and the velocity in the matrix and the fractures. Since the matrix and fracture gridcells have different geometrical dimensions (matrix gridcells are  $n$ -dimensional and fracture gridcells are  $(n-1)$ -dimensional), the governing equations are approximated separately. In the matrix domain (referred to by superscript  $m$ ), the equations describing the volumetric balance and velocity are given by:

$$\mathbf{v}_a^m = -\lambda_t^m \mathbf{K}^m \nabla \Phi_w^m, \quad (11)$$

$$\nabla \cdot (\mathbf{v}_a^m + \mathbf{v}_c^m) = F_t^m. \quad (12)$$

In the fractures, the governing equations are integrated along the fracture width  $\epsilon$ . The integrals are readily computed since the variations in potential and saturation are averaged across the fracture width. The fracture width is taken into consideration in the fracture–fracture flux and the accumulation term in the fracture gridcells. The equations in the fractures (referred to by the superscript  $f$ ) in  $(n-1)$ -dimensional are expressed by:

$$\mathbf{v}_a^f = -\lambda_t^f \mathbf{K}^f \nabla \Phi_w^f, \quad (13)$$

$$\nabla \cdot (\mathbf{v}_a^f + \mathbf{v}_c^f) = Q^f + F_t^f. \quad (14)$$

The transfer function  $Q^f$  in Eq. (14) accounts for the volumetric transfer across the matrix–fracture boundaries. This transfer function will be evaluated in the following section.

#### 4.1. Discretization in the matrix

The governing equations of the volumetric flow in the matrix expressed in Eqs. (11) and (12) are discretized separately by the hybridized MFE method with the lowest-order Raviart–Thomas space. The MFE discretization of the velocity expression in Eq. (11) in matrix gridcell  $K$  yields the explicit expression for the flux  $q_{a,K,E}^m$  across a gridcell-face  $E$  in terms of the cell-average potential  $\Phi_{w,K}^m$  and all the face-average potentials  $\Phi_{w,K,E}^m$  in all the faces of  $K$ , that is:

$$q_{a,K,E}^m = \alpha_{K,E}^m \Phi_{w,K}^m - \sum_{E' \in \partial K} \beta_{K,E,E'}^m \Phi_{w,K,E'}^m, \quad E \in \partial K, \quad (15)$$

where the terms  $\alpha_{K,E}^m$  and  $\beta_{K,E}^m$  are constants, independent of the potential and flux variables. Details are provided in Ref. [43].

The flux in Eq. (15) is written locally for all faces within each matrix gridcell. To link the gridcells in the mesh together, the following continuity conditions for the flux and the potential are imposed at each interface  $E$  of two neighboring gridcells  $K$  and  $K'$  (that is,  $E = K \cap K'$ ):



- If  $E$  is neither a fracture nor a barrier, the continuity of flux and potential is imposed.

$$\begin{cases} q_{a,K,E}^m + q_{a,K',E}^m = 0, \\ \Lambda_{w,K,E}^m = \Lambda_{w,K',E}^m = \Lambda_{w,E}^m. \end{cases} \quad (16)$$

- If  $E$  is a fracture, the total flux across both sides of the matrix–fracture interface defines the transfer function  $Q_{a,E}^f$  at  $E$ , which acts as a sink/source term. There is, however, continuity of the potential across the matrix–fracture interface  $E$  (see Fig. 3).

$$\begin{cases} q_{a,K,E}^m + q_{a,K',E}^m = Q_{a,E}^f, \\ \Lambda_{w,K,E}^m = \Lambda_{w,K',E}^m = \Phi_{w,E}^f. \end{cases} \quad (17)$$

- If  $E$  is a barrier, the flux across  $E$  is zero and face potentials  $\Lambda_{w,K,E}^m$  and  $\Lambda_{w,K',E}^m$  may not be equal.

$$\begin{cases} q_{a,K,E}^m = q_{a,K',E}^m = 0, \\ \Lambda_{w,K,E}^m \neq \Lambda_{w,K',E}^m. \end{cases} \quad (18)$$

We like to make the comment that Eq. (18) takes care of a barrier in simple way. In addition to the above conditions, the flux and potential at the domain boundaries are described by the Neumann or Dirichlet boundary conditions (see Ref. [43]). For the sake of simplicity, we assume that the domain boundaries are impermeable. From Eqs. (15)–(18), one can eliminate the flux variables and construct a system consisting of the unknowns; the fracture cell-potentials,  $\Phi_w^f$ , matrix cell-potentials,  $\Phi_w^m$ , and the matrix face-potentials,  $\Lambda_w^m$ . The system of equations corresponding to the matrix gridcells connected to fractures and those not connected to fractures are written separately as follows:

$$\begin{pmatrix} R^{T,m,m} \\ R^{T,m,f} \end{pmatrix} \Phi_w^m - \begin{pmatrix} M^{m,m} & M^{m,f} \\ M^{f,m} & M^{f,f} \end{pmatrix} \begin{pmatrix} \Lambda_w^m \\ \Phi_w^f \end{pmatrix} = \begin{pmatrix} 0 \\ Q^f \end{pmatrix}. \quad (19)$$

The system given in the above equations is split into two parts to explicitly show the connectivity at the matrix–fracture interfaces. Note that  $M^{m,f} = M^{f,m}$  in Eq. (19). The matrix–fracture volumetric transfer function  $Q^f$  will be eliminated later when we couple the flow between the matrix and the fractures. The definitions of the matrices in Eq. (19) are provided in Appendix A.

The next step is the integration of Eq. (12) over  $K$  and to obtain flux unknowns in terms of the potentials given in Eq. (15) [43], that is,

$$\alpha_K^m \Phi_{w,K}^m - \sum_{E \in \partial K} \alpha_{K,E}^m \Lambda_{w,K,E}^m = F_K^m, \quad (20)$$

where  $\alpha_K^m = \sum_{E \in \partial K} \alpha_{K,E}^m$ , and  $F_K^m = -\sum_{E \in \partial K} q_{c,K,E}^m + \int \int K(F_t^m)$  is a function of capillary pressure that will be discussed in section “Calculation of the capillary flux”.

In matrix form, Eq. (20) and the potential continuity equations given in Eqs. (16)–(18), yield:

$$D^m \Phi_w^m - (R^{m,m} \ R^{m,f}) \begin{pmatrix} \Lambda_w^m \\ \Phi_w^f \end{pmatrix} = F^m. \quad (21)$$

The diagonal matrix  $D^m$  in Eq. (21) is defined in Appendix A, and  $R^{m,m}$  and  $R^{m,f}$  appear in Eq. (19).

#### 4.2. Discretization in the fracture

In  $n - D$  space ( $n = 2, 3$ ), the fracture network is  $(n - 1) - D$ . The MFE formulation in the fracture network is basically similar to the conventional formulation in unfractured  $(n - 1) - D$  domain. There are, however, two differences: (1) the transfer function which acts as a sink/source in the fracture (see Fig. 4), (2) the fracture–fracture connectivity that may have multiple fracture–gridcells intersecting at the same interface as in Fig. 5. Similarly to the discretization in

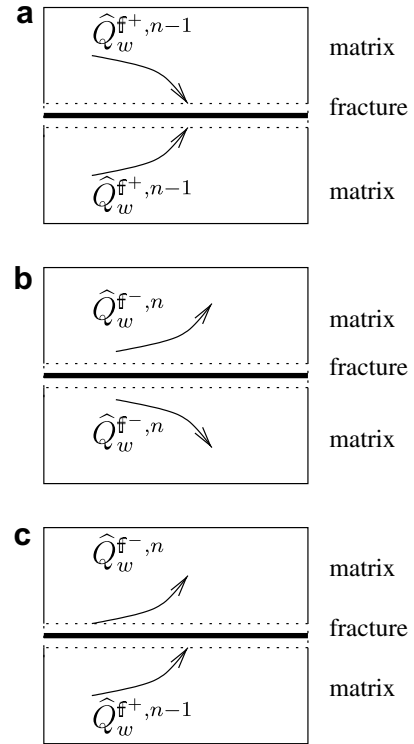


Fig. 4. Modeling of the flow in fractures in our proposed approach.

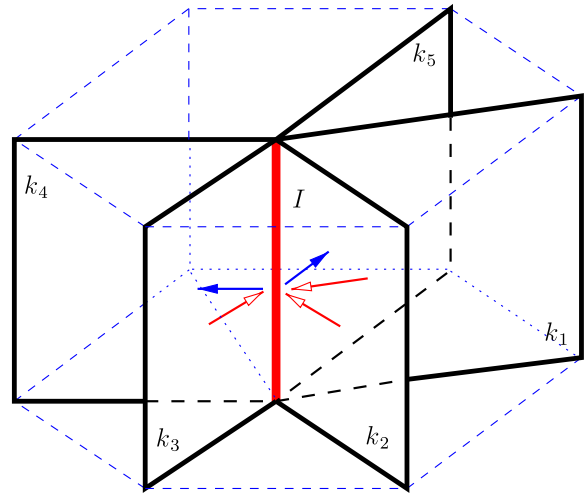


Fig. 5. Mesh with five intersecting fractures at  $I$ ; the fractures  $k_1, k_2, k_3$  are in the upstream, and  $k_4, k_5$  are in the downstream.

the matrix previously discussed, one discretizes the volumetric flow given in Eqs. (13) and (14) in the fractures. With the MFE discretization of Eq. (13) in a fracture gridcell  $k$  ( $k \in (n - 1) - D$  space), the flux  $q_{a,k,e}^f$  across an interface  $e$  ( $e \in (n - 2) - D$  space) of the fracture gridcell  $k$  becomes:

$$q_{a,k,e}^f = \alpha_{k,e}^f \Phi_{w,k}^f - \sum_{e' \in \partial k} \beta_{k,e,e'}^f \Lambda_{w,k,e'}^f, \quad e \in \partial k. \quad (22)$$

The constants  $\alpha_{k,e}^f$  and  $\beta_{k,e,e'}^f$  are similar to those defined in Eq. (15). Let  $n_e$  be the number of intersecting fractures at the interface  $e$ . The fracture–fracture interface  $e$  has a negligible volume, therefore, no accumulation is assumed and the potential continuity is imposed at  $e$ , that is,

$$\begin{cases} \sum_{i=1}^{n_e} q_{a,k_i,e}^f = 0, \\ \Lambda_{w,k_i,e}^f = \Lambda_{w,e}^f, \quad i = 1, \dots, n_e. \end{cases} \quad (23)$$

Using Eqs. (22) and (23), the flux unknown is eliminated and a system with the unknowns consisting of the fracture-gridcells potentials,  $\Phi_w^f$ , and the fracture-interfaces potentials,  $\Lambda_w^f$ , is obtained:

$$\tilde{R}^{T,f} \Phi_w^f - \tilde{M}^f \Lambda_w^f = 0. \quad (24)$$

The volumetric balance given in Eq. (14) is integrated over each fracture gridcell. In matrix form, a system similar to Eq. (21) is obtained:

$$\tilde{D}^f \Phi_w^f - \tilde{R}^f \Lambda_w^f = F^f + Q^f. \quad (25)$$

In the above equation,  $Q^f$  is the matrix–fracture transfer previously defined. The matrices  $\tilde{D}$ ,  $\tilde{R}^f$ , and  $F^f$  in Eq. (25), and  $\tilde{R}^{T,f}$  and  $\tilde{M}^f$  in Eq. (24) are defined in Appendix A.

#### 4.3. Combining the discretization in the matrix and fractures

The MFE formulations of the volumetric flow in the matrix and fractures are coupled through the matrix–fracture transfer function and the continuity of the potential given in Eq. (17). By subtracting Eq. (25) from the second equation in Eq. (19), the transfer function  $Q^f$  cancels out. The resulting equation from the first equation in Eq. (19) and Eqs. (21) and (24) becomes:

$$\begin{pmatrix} D^m & -R^{m,m} & -R^{m,f} & 0 \\ -R^{T,m,m} & M^{m,m} & M^{m,f} & 0 \\ -R^{T,m,f} & M^{m,f} & (M^{f,f} + \tilde{D}^f) & -\tilde{R}^f \\ 0 & 0 & -\tilde{R}^{T,f} & \tilde{M}^f \end{pmatrix} \begin{pmatrix} \Phi_w^m \\ \Lambda_w^m \\ \Phi_w^f \\ \Lambda_w^f \end{pmatrix} = \begin{pmatrix} F_w^m \\ 0 \\ -F_w^f \\ 0 \end{pmatrix}. \quad (26)$$

The matrix  $D^m$  is diagonal and invertible, therefore, a simple Gaussian elimination can be performed to eliminate the unknown  $\Phi_w^m$ . The final linear system reads as:

$$\begin{pmatrix} A^{m,m} & A^{m,f} & 0 \\ A^{m,f} & A^{f,f} & -\tilde{R}^f \\ 0 & -\tilde{R}^{T,f} & \tilde{M}^f \end{pmatrix} \begin{pmatrix} \Lambda_w^m \\ \Phi_w^f \\ \Lambda_w^f \end{pmatrix} = \begin{pmatrix} V^m \\ V^f \\ 0 \end{pmatrix}. \quad (27)$$

The sought unknowns are, therefore, the traces of the wetting-phase potential in the matrix,  $\Lambda_w^m$ , the fracture gridcell potentials,  $\Phi_w^f$ , and the traces of the potential in the fracture network,  $\Lambda_w^f$ . The system in Eq. (27) has a size equal to the number of mesh interfaces plus the number of fracture–fracture interfaces; it is sparse, symmetric and positive definite. There is no particular difficulty in constructing the system in Eq. (27). A simple example for a 2D fractured domain is given in Appendix B to show the structure of the linear system. After solving Eq. (27), the matrix potentials and the flux in the matrix and fracture network are calculated locally from the first equation in Eq. (26), and Eqs. (15) and (22).

#### 4.4. Calculation of the capillary flux

The degenerate flux from the capillary pressure and gravity,  $q_c$ , in the right-hand side of Eqs. (15) and (22) is written in terms of the cell capillary potential  $\Phi_c$  and the face capillary potential  $\Lambda_c$  in the matrix and fractures. In a matrix gridcell,  $K$ , the flux across an interface  $E$  is given by Hoteit and Firoozabadi [43]:

$$q_{c,K,E}^m = \hat{\alpha}_{K,E}^m \Phi_{c,K}^m - \sum_{E' \in \partial K} \hat{\beta}_{K,E,E'}^m \Lambda_{c,K,E'}^m, \quad E \in \partial K. \quad (28)$$

Similarly to Eq. (28), in a fracture gridcell,  $k$ , the flux across an interface  $e$  is given by:

$$q_{c,k,e}^f = \hat{\alpha}_{k,e}^f \Phi_{c,k}^f - \sum_{e' \in \partial k} \hat{\beta}_{k,e,e'}^f \Lambda_{c,k,e'}^f, \quad e \in \partial k. \quad (29)$$

By imposing the continuity of capillary pressure and flux at the matrix–matrix and fracture–fracture interfaces, the flux unknowns  $q_{c,K,E}^m$  and  $q_{c,k,e}^f$  are eliminated, and the following system is obtained:

$$\begin{pmatrix} \hat{M}^m & 0 \\ 0 & \hat{M}^f \end{pmatrix} \begin{pmatrix} \Lambda_c^m \\ \Lambda_c^f \end{pmatrix} = \begin{pmatrix} \hat{V}^m \\ \hat{V}^f \end{pmatrix} - \begin{pmatrix} \hat{R}^{T,m} \Phi_c^m \\ \hat{R}^{T,f} \Phi_c^f \end{pmatrix}. \quad (30)$$

The matrices in the above equation are defined in Appendix A. The capillary potentials  $\Phi_c^m$  and  $\Phi_c^f$  in the right-hand side of Eq. (30) are calculated by using the capillary pressure functions and the wetting-phase saturations from the previous time step. The capillary pressure at the fracture gridcells are also calculated from the corresponding saturations. The system in Eq. (30) is diagonal per block and the matrices  $\hat{M}^m$ ,  $\hat{M}^f$  are symmetric and positive definite, therefore, solvers such as preconditioned-conjugate-gradient (PCG) can be used efficiently.

### 5. Approximation of the wetting-phase saturation

As we did for the volumetric flow equation, the saturation equation describing the mass conservation is written separately in the matrix and fractures. In the matrix, the wetting-phase saturation is defined by  $S_w^m$  and the governing equation is given by:

$$\phi^m \frac{\partial S_w^m}{\partial t} + \nabla \cdot (f_w^m \mathbf{v}_a^m) = F_w^m. \quad (31)$$

The discontinuous Galerkin (DG) method is used to approximate Eq. (31) with an explicit, second-order Runge–Kutta time scheme. A multidimensional slope limiter [42] is applied in a post-processing step to remove potential oscillations in the saturation. A detailed description is provided in Ref. [43].

The saturation equation in the fracture network is written as:

$$\phi^f \frac{\partial S_w^f}{\partial t} + \nabla \cdot (f_w^f \mathbf{v}_a^f) = \hat{Q}_w^f + F_w^f. \quad (32)$$

The sink/source term,  $\hat{Q}_w^f$ , in the above equation is equal to the volumetric transfer function,  $Q^f$  in Eq. (14), multiplied by the wetting-phase fractional flow function  $f_w$ . From the assumption of incompressibility of the fluids,  $\hat{Q}_w^f$  represents the mass transfer function through the matrix–fracture interfaces. Because the flow in the fracture network can be much faster than that in the matrix, a first-order implicit time scheme is used to approximate the time operator in Eq. (32). This approach removes the CFL restriction on the time step in the fracture network and allows different time steps in the matrix and the fractures. Unlike the approximations in the matrix, a first-order spatial scheme is used for the saturation equation in the fractures. As a result, one may expect more numerical dispersion in fracture saturation, however, this may not have a significant influence as a second-order method is used in the matrix. We do not use an implicit DG method in the fracture for its expensive computational overhead. The first-order temporal and spatial discretizations of Eq. (32) in a fracture gridcell  $k$  at a time step  $n$  reads as:

$$\phi_k^f \frac{S_w^{f,n} - S_w^{f,n-1}}{\Delta t} + \sum_{e \in \partial k} f_{w,e}^f q_{a,k,e}^{f,n} = \underbrace{\hat{Q}_w^{f+,n-1} + \hat{Q}_w^{f-,n}}_{\hat{Q}_w^{f,n}} + F_{w,k}^{f,n}. \quad (33)$$

The second term on the left-hand side of Eq. (33) represents the net fracture–fracture flux. The volumetric flux  $q_{a,k,e}^{f,n}$  is calculated in a preprocessing step from the MFE approximations, previously discussed. The matrix–fracture mass transfer function on the right-hand side of Eq. (33) is split into two parts that are approximated differently according to the flow direction between the fracture and the two adjacent matrix gridcells. The notation  $\hat{Q}_w^{f+,n-1}$  refers to a source term and  $\hat{Q}_w^{f-,n}$  refers to a sink term for the fracture gridcell. We distinguish three possible cases as follows:

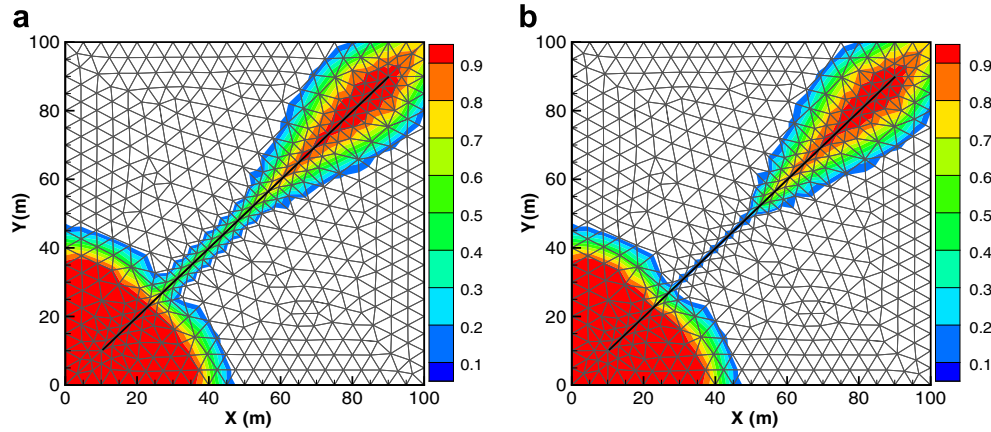


**Fig. 6.** Water saturation contours at PVI = 0.5: with and without the cross-flow equilibrium,  $\kappa = 0.4$ ; Example 1. (a) With cross-flow equilibrium; (b) without cross-flow equilibrium.

- If the two adjacent matrix gridcells are in the upstream of the fracture, as appears in Fig. 4a, then  $\hat{Q}_w^{f,n} = 0$  and the total source term for the fracture,  $\hat{Q}_w^{f,n-1}$ , is approximated explicitly in time.
- If the two adjacent matrix gridcells are in the downstream of the fracture, as appears in Fig. 4b, then  $\hat{Q}_w^{f,n-1} = 0$  and the total sink term for the fracture,  $\hat{Q}_w^{f,n}$ , is approximated implicitly in time.
- If one matrix gridcell is in the upstream and the other in the downstream (see Fig. 4c), then the source term is approximated explicitly and the sink term implicitly.

The approach presented above is locally conservative in the matrix and fractures. The system of equations given in Eq. (33) is linearized by the Newton–Raphson (NR) method. If the NR method fails to converge for a certain time step, one can cut the time step and does multiple iterations in the fractures without reducing the global time step in the matrix. The time step in our method is constrained by a CFL condition in the matrix where the explicit time method is used and by the nonlinearity (Newton iterations) owing to the flow interaction at the matrix–fracture interfaces. A simple dynamic time-step algorithm is adopted, where the time step is controlled by the change in saturation in the gridblocks within the previous time step and the number of Newton iterations required for convergence.

The mobilities at the fracture–fracture interface are approximated by the conventional single-point upstream-weighting technique. An important point to be addressed next is how to define the upstream-weighting in case of multiple intersecting fractures, where one fracture gridcell may have multiple upstream fractures.

### 5.1. Upstream-weighting at multiple intersection fractures

In the past, we developed a technique for multiple intersecting fractures in 2D space [52,53]; the extension to fractures in 3D domain is straightforward. Let  $I$  be the interface (line) connecting  $N_I$

fracture gridcells,  $k_i$ ,  $i = 1, \dots, N_I$ , as sketched in Fig. 5. The purpose is to evaluate the mobility at  $I$  which is given by fractional flow function  $f_{w,I}$  (see Eq. (33), for simplicity we drop the notation  $\dagger$ ). In each fracture cell  $k_i$ , the fractional flow function and the volumetric flux

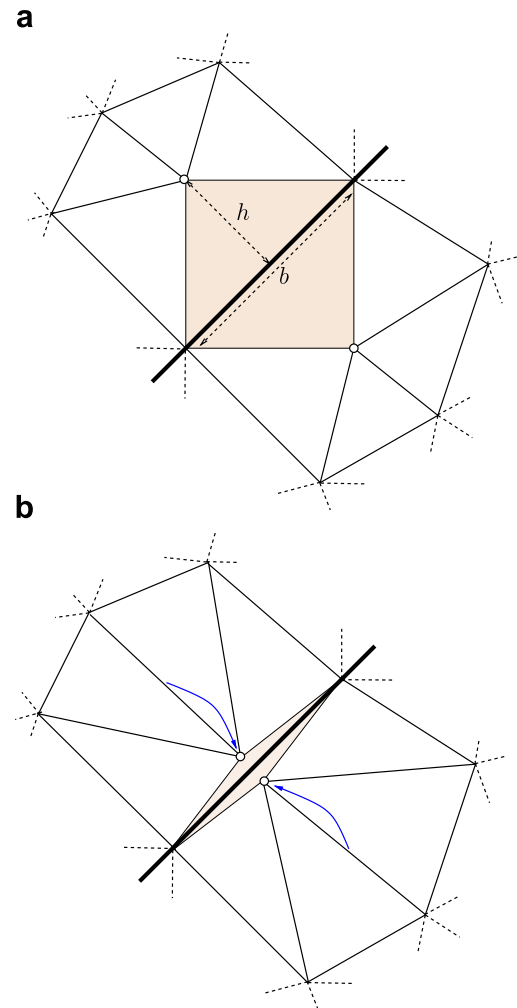


**Fig. 7.** Matrix elements with different aspect ratios; Example 1. (a)  $\kappa = \frac{2h}{b} = 1.0$ ; (b)  $\kappa = \frac{2h}{b} = 0.1$ .

**Table 1**

Relevant data for Examples 1 and 2

Domain dimensions: 100 m × 100 m
Matrix properties: $\phi^m = 0.2$ , $K^m = 1$ md
Fracture properties: $\phi^f = 1.0$ , $K^f = 10^6$ md, $\epsilon = 1$ mm
Fluid properties: $\mu_w = \mu_n = 1$ cp, $\rho_w = \rho_n = 1000$ kg/m <sup>3</sup>
Relative permeabilities: linear (Eq. (39))
Capillary pressure: neglected
Residual saturations: $S_{rw} = 0.0$ , $S_m = 0.0$
Injection rate: 0.05 PV/day
Mesh number: $\approx 1000$ triangles

at  $I$  are denoted by  $f_{w,k_i}$  and  $q_{a,w,k_i}$ . According to the signs of the fluxes, influx or efflux at  $I$ , we define an integer  $\ell$  ( $0 < \ell < N_I$ ), such that:

$$\begin{aligned} q_{a,w,k_i} &> 0 \quad \text{for } 0 < i \leq \ell \text{ (influx),} \\ q_{a,w,k_i} &\leq 0 \quad \text{for } \ell < i < N_I \text{ (efflux).} \end{aligned} \quad (34)$$

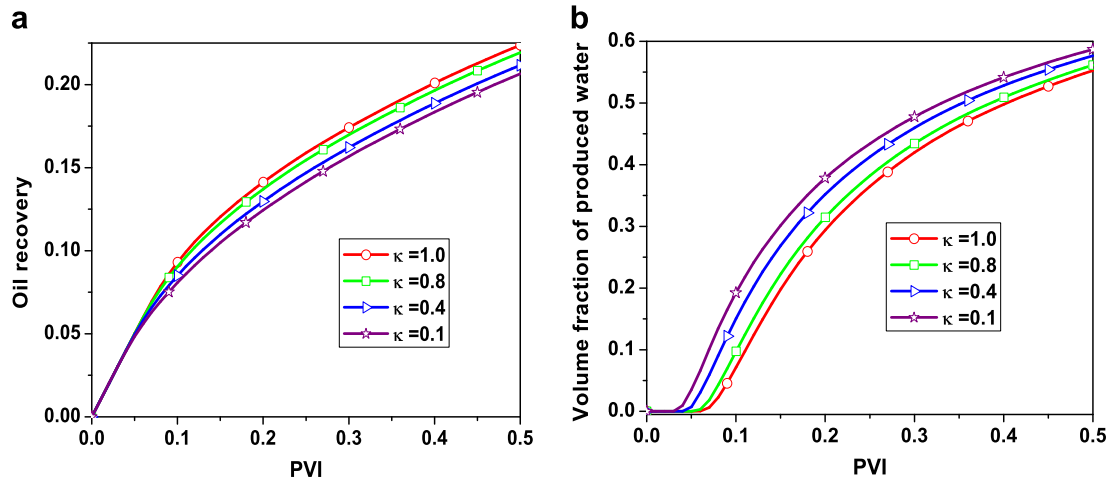


Fig. 8. Oil recovery and water production versus PVI for different mesh aspect ratios with the cross-flow equilibrium; Example 1. (a) Oil recovery; (b) water production.

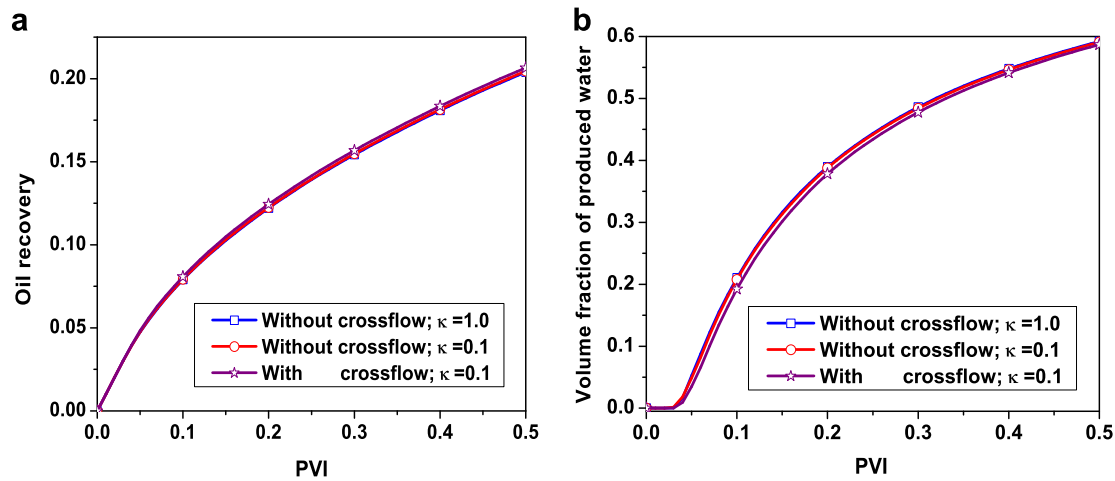


Fig. 9. Oil recovery and water production versus PVI for different mesh aspect ratios with and without the cross-flow equilibrium; Example 1. (a) oil recovery; (b) water production.

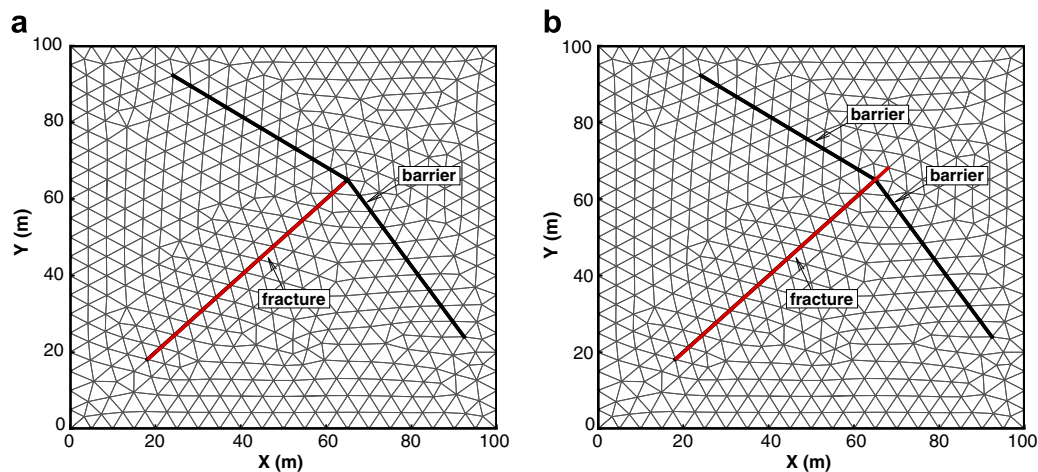


Fig. 10. Gridding of the domain with one fracture and one barrier; Case I: the fracture does not cross the barrier; Case II: the fracture crosses the barrier; Example 2. (a) Case I; (b) Case II.



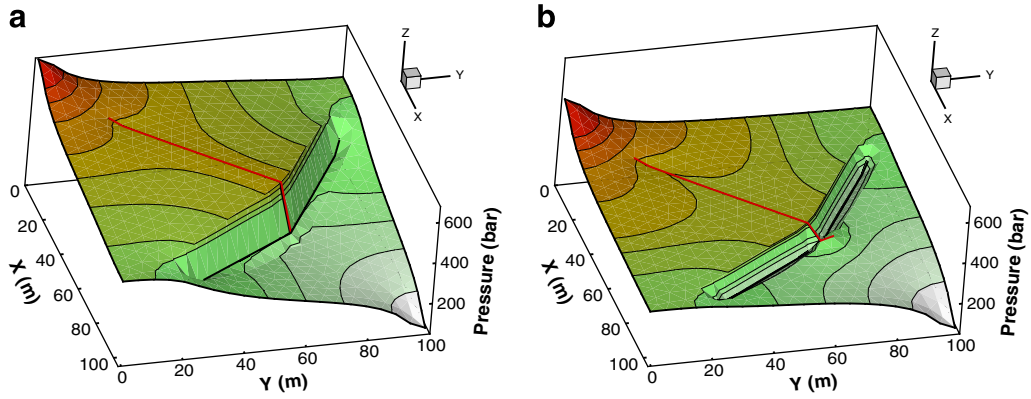


Fig. 11. Pressure contours for Cases I and II; PVI = 0.5; Example 2. (a) Case I; (b) Case II.

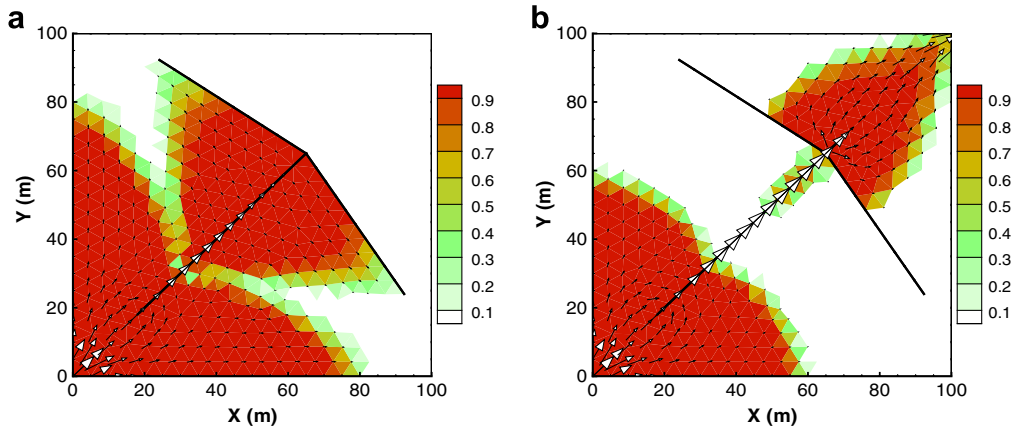


Fig. 12. Water saturation contours for Cases I and II; PVI = 0.5; Example 2. (a) Case I; (b) Case II.

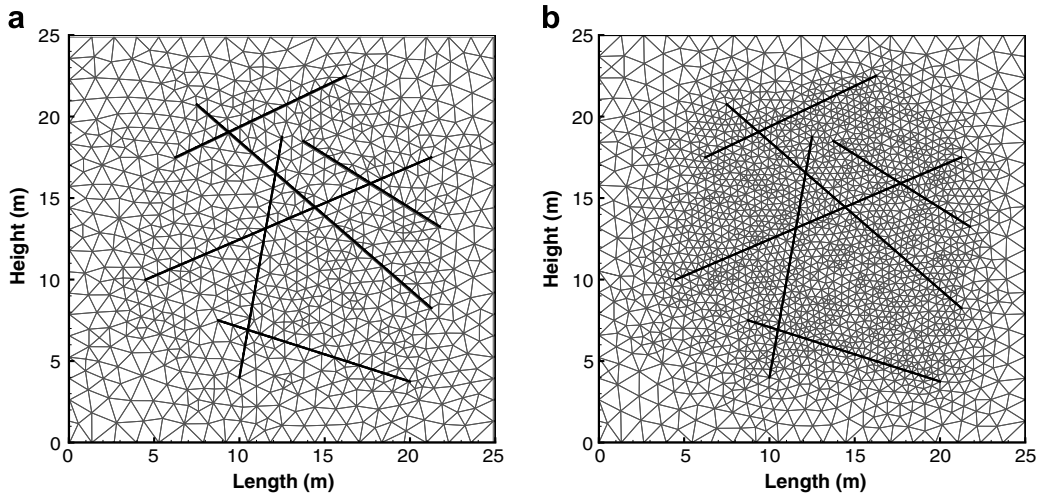


Fig. 13. Triangulations of the fracture domain; Example 3. (a) Coarse:  $N_k^m = 1718$ ,  $n_k^i = 104$ ; (b) fine:  $N_k^m = 4667$ ,  $N_k^i = 191$ .

**Table 2**  
Relevant data for Example 3

Domain dimensions: 25 m × 25 m
Matrix properties: $\phi^m = 0.2$ , $K^m = 1$ md
Fracture properties: $\phi^f = 1.0$ , $K^f = 8 \times 10^5$ md, $\epsilon = 0.1$ mm
Fluid properties: $\mu_w = 1$ cp, $\rho_w = 1000$ kg/m <sup>3</sup> , $\mu_n = 0.45$ cp, $\rho_n = 660$ kg/m <sup>3</sup>
Injection rate: 0.0027 PV/day
Mesh number: 1718 (coarse) and 4667 (fine) triangles

Note that, an integer  $\ell$  that satisfies Eq. (34) does always exist. By writing the total volumetric balance and the total mass balance at  $I$ , one gets,

$$\sum_{i=1}^{\ell} q_{a,w,k_i} = - \sum_{i=\ell+1}^{N_I} q_{a,w,k_i}, \quad (35)$$

$$\sum_{i=1}^{\ell} f_{w,k_i} q_{a,w,k_i} = - \sum_{i=\ell+1}^{N_I} f_{w,I} q_{a,w,k_i} = -f_{w,I} \sum_{i=\ell+1}^{N_I} q_{a,w,k_i}. \quad (36)$$

**Table 3**  
Relative permeabilities and capillary pressure in the matrix: Example 3

$S_w$	$k_w$	$k_n$	$p_c$ (bar)
0	0	0.6	1
0.1	4.5E–6	0.412	0.642
0.2	1.4E–4	0.264	0.434
0.3	0.001	0.163	0.3124
0.4	0.004	0.089	0.2261
0.5	0.014	0.041	0.1592
0.6	0.035	0.015	0.1045
0.7	0.075	0.003	0.0582
0.8	0.148	1.2E–4	0.018
0.85	0.200	0	0

**Table 4**  
Relative permeabilities and capillary pressure in the fractures: Example 3

$S_w$	$k_w$	$k_n$	$p_c$ (bar)
0	0	1	1
0.1	0.118	0.882	0.080
0.2	0.235	0.765	0.040
0.3	0.353	0.647	0.025
0.5	0.588	0.412	0.010
0.6	0.706	0.294	0.005
0.7	0.824	0.176	1.E–3
0.85	1	0	0

In Eq. (36),  $f_{w,I}$ , which refers to the mobility at  $I$ , is equal to the upstream mobility for the effluxes. From Eqs. (35) and (36),  $f_{w,I}$  can be readily calculated:

$$f_{w,k_i} = \frac{\sum_{i=1}^{\ell} f_{w,k_i} q_{a,w,k_i}}{\sum_{i=1}^{\ell} q_{a,w,k_i}}. \quad (37)$$

The expression for the mobility in Eq. (37) is a generalization of the conventional two-point upstream-weighting technique.

## 6. Numerical examples

The combined MFE-DG method with capillary effect was validated using analytical solutions for two-phase flow in unfractured media. We demonstrated that the algorithm enjoys accuracy and robustness especially in highly heterogeneous media with unstructured gridings [43]. In fractured media, the MFE-DG associated with the cross-flow equilibrium has been validated with the single-porosity model [53]. In this work, we provide four examples of various degrees of complexity. In the first example, we present results demonstrating that our method is not sensitive to the size of the matrix gridcells next to the fractures. The previous works in the literature invoking the concept of cross-flow equilibrium between the fractures and the adjacent rock matrix depend on the matrix gridding. The second example shows the flexibility of our proposed model in numerical simulation of two-phase flow in porous media composed of a fracture and a barrier. The third example investigates the effect of the fracture capillary pressure on the fluid flow. The last example demonstrates the efficiency of our method in a large 3D problem with layering, barriers, and fractures. We would like to point that the gridding for all the problems is by no means optimal. The selection shows powerful features of the algorithm. All runs were performed on an 1.8 GHz Intel-Centrino PC with 1 GB of RAM.

### 6.1. Example 1: mesh sensitivity

In this example, we examine the dependency of our model on the size of the matrix gridcells in the vicinity of the fractures. We consider a 2D horizontal porous medium of dimensions

(100 m × 100 m) with one fracture along the diagonal, as shown in Fig. 6. The domain is initially saturated with oil. Water is injected at the lower left corner to produce oil at the opposite corner. The fluid and medium properties are provided in Table 1. The domain is discretized into a mesh with about 1000 triangular matrix gridcells and 20 fracture gridcells (segments). We define an aspect ratio  $\kappa$  for the matrix gridcells next to the fractures by  $\kappa = 2h/b$ , where  $h$  is the triangle height, and  $b$  is the base. Fig. 7a shows a mesh where the aspect ratio is one. In Fig. 7b, the aspect ratio is reduced to 0.1 by dragging the nodes of the triangles facing the fractures closer to its base (that is, the fracture). The aspect ratio of the mesh is, therefore, modified by changing the locations of some nodes without changing their number.

Fig. 6 shows the water saturation profiles with and without the cross-flow equilibrium assumption. The former appears to be more dispersive close to the fracture. Oil recovery and water breakthrough obtained with the cross-flow equilibrium assumption for different aspect ratios are plotted in Fig. 8. Large matrix gridcells next to the fractures, that correspond to large aspect ratios, delay water breakthrough and result in overestimation of the oil recovery. The results show that convergence is obtained with a small aspect ratio (about 0.1) indicating that the matrix gridcells should be relatively small. On the other hand, our new model, shows almost identical results for aspect ratios of 1.0 and 0.1 (Fig. 9). Fig. 9 also shows that the results obtained with cross-flow equilibrium with fine matrix gridcells ( $\kappa = 0.1$ ) converges to the results by our method with coarse matrix gridcells ( $\kappa = 1$ ). We also note that both methods need comparable CPU time on the same mesh, however, our method with  $\kappa = 1$  is nearly one order of magnitude faster than the method with  $\kappa = 0.1$ .

### 6.2. Example 2: flexibility in modeling fractures and barriers

In this example, we demonstrate the flexibility of the MFE-DG method in modeling fractures and barriers. We consider a 2D rectangular domain (100 m × 100 m) initially saturated with oil. The injector and producer locations are as in Example 1; the relevant data are provided in Table 1. One fracture and one barrier are embedded in the porous medium; two cases, I and II, are distinguished. In Case I, the fracture touches the barrier but does not cross it (see Fig. 10a). In Case II, the fracture intersects the barrier and crosses it (Fig. 10b).

The fracture–barrier intersection point in Case I has a dual role. The precise modeling by the Galerkin FE method with consideration of the degrees of freedom at the mesh nodes, is not straightforward. In Case II, the injected fluid flows through the barrier via a single point located at the fracture–barrier intersection. Modeling this case is a challenge for the CVFE method due to consideration of the degrees of freedom at the center of the control-volumes. We model in a simple way both cases without a special treatment. The implementation of simple expressions in Eqs. (17) and (18) in the MFE-DG method provides the tool to model two-phase flow with capillarity and gravity in complex media containing fractures (Eq. (17)) and barriers (Eq. (18)). Fig. 11 depicts the pressure contours with discontinuity at the barrier (Fig. 11a, Case I) and pressure continuity for the fracture crossing the barrier (Fig. 11b, Case II). Results for water saturations at PVI = 0.5 for Cases I and II are plotted in Fig. 12a and b, respectively.

### 6.3. Example 3: capillary pressure effect

In the past, Karimi-Fard and Firoozabadi [23] have used the domain in Fig. 13 to study the effect of capillary pressure on water injection in fractured media. In this example, we use our method to provide a comprehensive study in terms of model efficiency and capillary pressure effect. The domain with the fracture net-

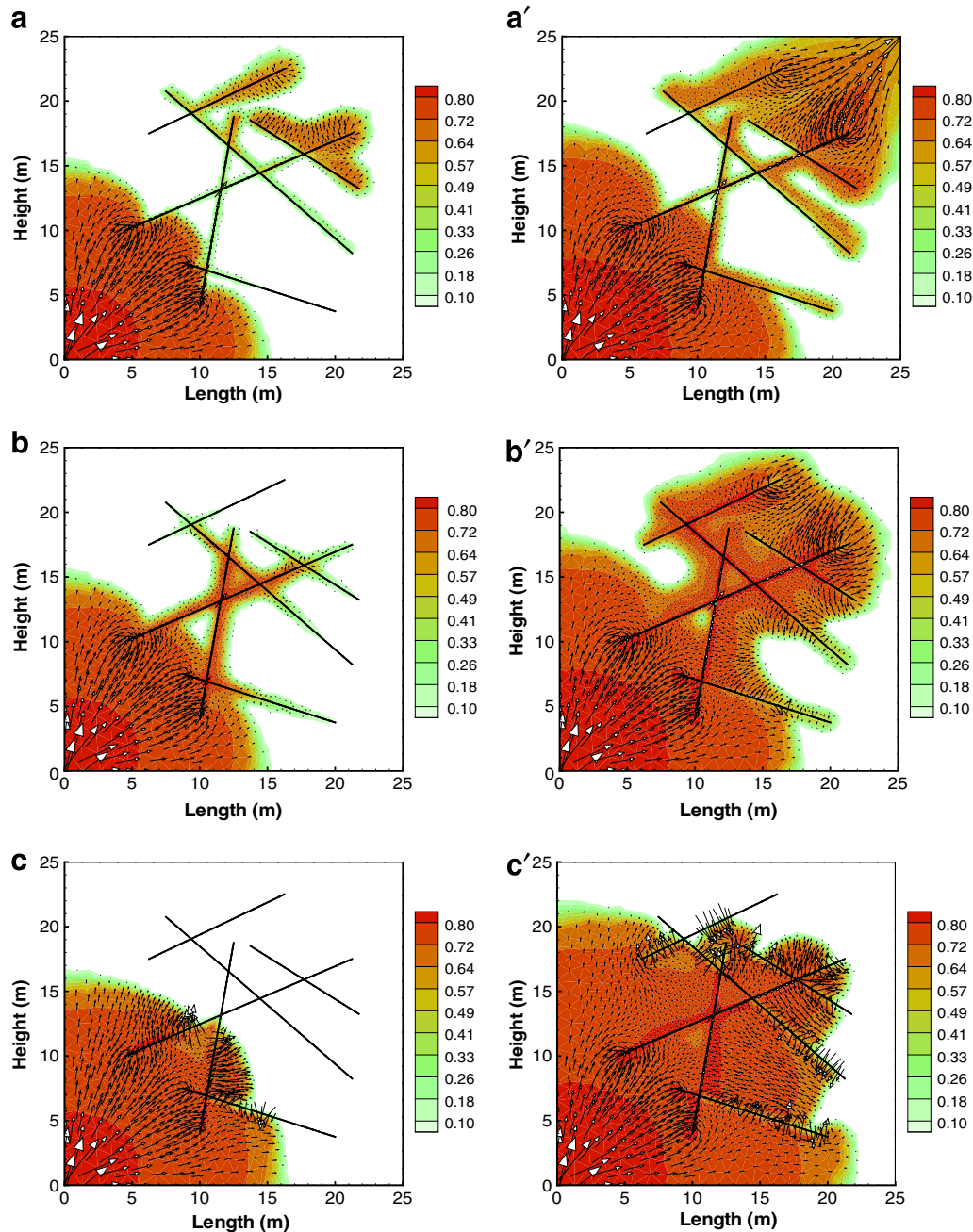


**Fig. 14.** Water saturation contours and water velocity field for cases I, II, and III at PVI = 0.25 and PVI = 0.50; Example 3. (a) PVI = 0.25:  $p_c^m = 0$ ,  $p_c^f = 0$  (Case I); (a') PVI = 0.50:  $p_c^m = 0$ ,  $p_c^f = 0$  (Case I); (b) PVI = 0.25:  $p_c^m \neq 0$ ,  $p_c^f \neq 0$  (Case II); (b') PVI = 0.50:  $p_c^m \neq 0$ ,  $p_c^f \neq 0$  (Case II); (c) PVI = 0.25:  $p_c^m \neq 0$ ,  $p_c^f = 0$  (Case III); (c') PVI = 0.25:  $p_c^m \neq 0$ ,  $p_c^f = 0$  (Case III).

work is sketched in Fig. 13a and b corresponding to a coarse and a fine grid. The relative permeability and capillary pressure curves in the matrix and fractures are given in Tables 3 and 4, respectively. Other relevant data are provided in Table 2. We investigate the effect of capillary pressure on flow by considering three cases. In Case I, the capillary pressures in the matrix ( $p_c^m$ ) and in the fracture ( $p_c^f$ ) are neglected (that is,  $p_c^m = p_c^f = 0$ ). In Case II, both capillary pressures are nonzero, as provided in Tables 3 and 4. In Case III, only the fracture capillary pressure is zero and that of the matrix is given in Table 3.

In Fig. 14, we show the water saturation distributions and water velocity profiles for the three cases at PVI = 0.25 and PVI = 0.5 on the fine grid. In Case I (Fig. 14a and a'), water flows very quickly through the fractures and leads to early breakthrough. In Case II

(Fig. 14b and b'), however, the effect of capillary-pressure contrast at the matrix–fracture interface delays breakthrough. Note that due to capillary cross-flow, the displacement process becomes much more efficient in Case II than in Case I.

As the contrast of capillary pressure increases in Case III (Fig. 14c and c'), the fractures permeability has little influence on water mobility due to very large capillary effect when water saturation in the matrix is much lower in the matrix than in the fracture. Although, the fracture absolute permeability is orders of magnitudes greater than that in the matrix, water in the fractures and the surrounding matrix flows with comparable speed. The contrast in capillary pressure at the fracture–matrix interface creates a significant cross-flow via the water velocity vectors laterally crossing the fractures (see Fig. 14c and c'). The oil recovery and water



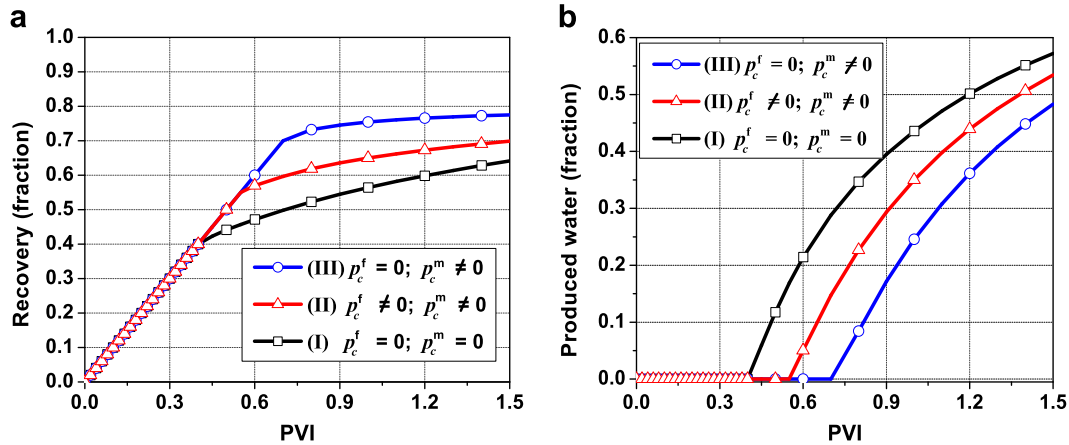


Fig. 15. Oil recovery and water production versus PVI for the three cases I, II, and III; Example 3. (a) Oil recovery; (b) water production.

Table 5

Relevant data for Example 4

Domain dimensions:  $1000 \text{ m} \times 300 \text{ m} \times 250 \text{ m}$   
 Matrix properties:  $\phi^m = 0.2$ ,  $K^m = \{20 \text{ md}, 1 \text{ md}, 10 \text{ md}\}^a$   
 Fracture properties:  $\phi^f = 1.0$ ,  $K^f = 10^5 \text{ md}$ ,  $\epsilon = 1 \text{ mm}$   
 Fluid properties: as in Example 3  
 Relative permeabilities (layers): Eq. (39) with  $m_w = \{2, 3, 2\}$ ;  
 $m_n = \{3, 3, 2\}^a$ ,  $S_{rn} = 0$ ;  $S_{rw} = 0.25$  (all layers)  
 Relative permeabilities linear (fractures): (Eq. (39));  $S_{rn} = S_{rw} = 0$   
 Capillary pressure (Case I): neglected  
 Capillary pressure (Case II):  $B_f = 0.01$ ,  $B_m = \{1, 5, 2\}^a$  bar  
 Injection rate:  $10^{-4}$  PV/day  
 Mesh number:  $\approx 8500$  prisms

<sup>a</sup> In layers 1 (top), 2 and 3, respectively.

Table 6

CPU time in minutes for Examples 3 and 4

	Example 3 (coarse)	Example 3 (fine)	Example 4
Zero capillarity	0.9	3.7	56
Nonzero capillarity	1.5	7.6	98

breakthrough versus PVI for the three cases are plotted in Fig. 15. It is obvious that capillary pressure contrast improves the recovery and delays the breakthrough. The capability to explicitly describe the matrix–fracture cross-flow due to capillary pressure contrast is a significant feature of our method. The results from the fine and coarse grids are almost the same. The CPU times on both grids

for Cases I and II are shown in Table 6. The CPU time in Case III is about 20% more than in Case II.

#### 6.4. Example 4: complex 3D media with layers, faults, and fractures

In this example, we consider a 3D layered tilted domain ( $1000 \text{ m} \times 300 \text{ m} \times 250 \text{ m}$ ), as appears in Fig. 16a. The medium has two barriers and several intersection fractures (Fig. 16b). The layer thicknesses from top to bottom are 30 m, 40 m, and 30 m, respectively. The injector is located at the bottom corner of the medium (at  $(0, 0, 0)$ ) and the producer at the opposite top corner (at  $(1000 \text{ m}, 300 \text{ m}, 250 \text{ m})$ ). The domain is discretized into an unstructured mesh of 8500 matrix gridcells (prisms) (Fig. 16a). The number of fracture gridcells (quadrilaterals) is nearly 1700. In Ref. [43], we showed the applicability of the MFE-DG method on different discretizations in 3D. The rock properties, and relative permeability functions used in the layers and the fractures are provided in Table 5. The relative permeabilities and the capillary pressure are given by:

$$k_{rw} = S_e^{m_w}; \quad k_{rn} = (1 - S_e)^{m_n}, \quad (38)$$

$$p_c = -B \ln(S_e), \quad (39)$$

where  $m_w$  and  $m_n$  are defined in Table 5, and  $S_e$  is the normalized saturation defined in terms of  $S_{rw}$  and  $S_{rn}$ , which are the residual saturations for the wetting and non-wetting phases, respectively:

$$S_e = \frac{S_w - S_{rw}}{1 - S_{rw} - S_{rn}}. \quad (40)$$

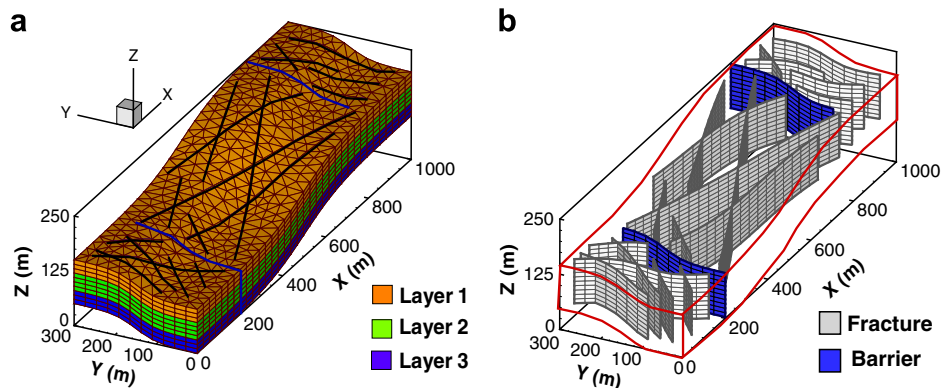


Fig. 16. Discretization of the layered domain and the embedded fractures and barriers; Example 4. (a) 3D layered domain; (b) 2D fractures and barriers.



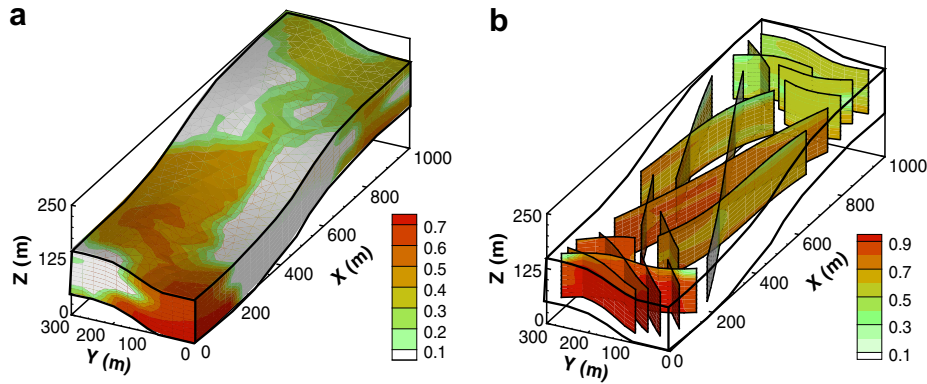


Fig. 17. Water saturation profiles in the matrix and fractures at PVI = 0.25, zero capillary pressure; Example 4. (a) Matrix; (b) fractures.

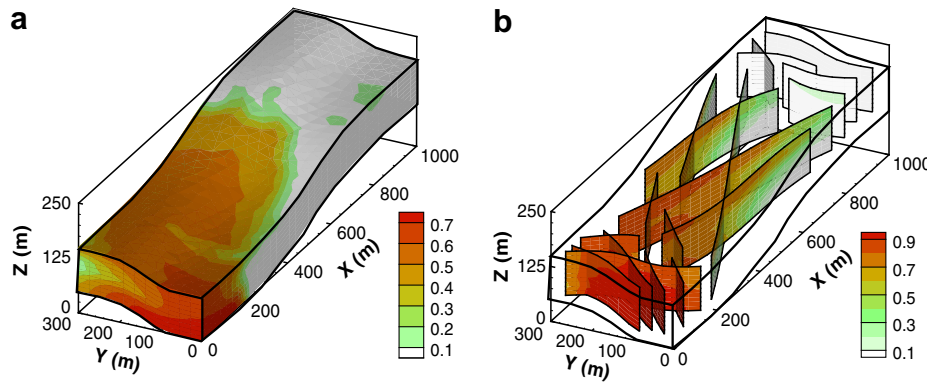


Fig. 18. Water saturation profiles in the matrix and fractures at PVI = 0.25, nonzero capillary pressure; Example 4. (a) Matrix; (b) fractures.

Two cases with zero and non-zero capillary pressures are considered. Water saturation profiles in the matrix and fractures for both cases are shown in Figs. 17 and 18. Capillary pressure reduces water velocity in the fractures and, therefore, improves recovery, as shown in Fig. 19. We note that the use of the implicit time scheme with the desirable feature of smaller time steps in the fractures without reducing the time step in the matrix has improved significantly the computational efficiency. In addition to the above examples, we have tested the proposed method for a variety of

other problems. All the examples show powerful features of the algorithm. We have also compared the simulation results and measured data from water injection in 3D oil-saturated media. The agreement is excellent. The comparison between simulation and data will be made in a future publication.

## 7. Conclusions

A numerical model based on the combined MFE and DG methods is introduced to simulate incompressible two-phase flow in multidimensional fractured media. The main features of our new method are:

- The saturation discontinuity at the matrix–fracture interface from the capillary pressure contrast is properly described.
- A new approach is introduced without the use of the cross-flow equilibrium between the fractures and the adjacent matrix blocks. The continuity of pressure is only imposed at the matrix–fracture interface. This approach allows relatively large matrix gridcells next to the fractures.
- The hybrid time scheme (implicit in the fracture and explicit in the matrix) alleviates the restriction on the size of the time step from the CFL condition.
- We provide a generalized upstream weighting technique to approximate the mobilities at the fracture intersections.
- The method has the flexibility to describe complicated fractured domains with barriers.
- The MFE-DG method has other advantages in reducing the numerical dispersion and convergence on unstructured meshes of low qualities [43].

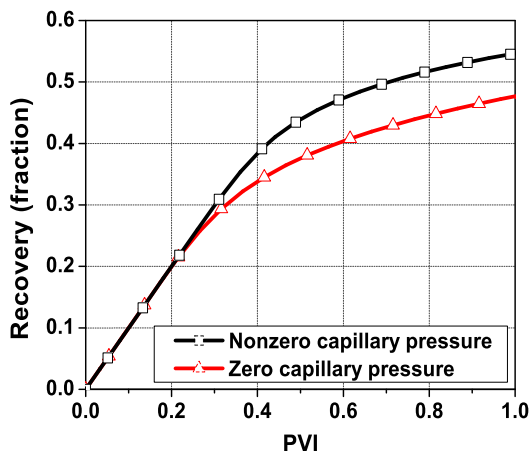


Fig. 19. Oil recovery versus PVI with zero and nonzero capillary pressure; Example 4.

## Acknowledgement

This work was supported by the member companies of the Reservoir Engineering Research Institute (RERI). Their support is greatly appreciated.

## Appendix A. The MFE discretization

In the MFE method, the 3D fractured domain is discretized into a mesh composed of hexahedrons, tetrahedrons, or prisms. The fractures can, therefore, be quadrilaterals or triangles. Hybrid mesh with different geometrical gridcells can be readily handled by the MFE method (see Appendix B).

We define the following notation in the matrix and fractures:

- $N_K^m$ : number of gridcells in the matrix.
- $n_K^m$ : number of faces of the matrix gridcell  $K$ .
- $N_E^m$ : number of non-fracture interfaces in mesh.
- $N_k^f$ : number of gridcells in the fracture network.
- $n_k^f$ : number of edges of the fracture gridcell  $k$ .
- $N_e^f$ : number of fracture–fracture interfaces in the fracture network.

The local integration of the velocity equation in the matrix and fracture gridcells yield to two types of elementary matrices:

In a matrix gridcell  $K$ , one gets an  $n_K^m \times n_K^m$  symmetric positive definite (SPD) matrix  $A_K^m$  in terms of the permeability tensor  $\tilde{\mathbf{K}}^m$  and the  $RT_0$  basis function  $\mathbf{w}_K^m$  [43], such that:

$$A_K^m = [A_{K,E,E'}^m]_{E,E' \in \partial K}; \quad A_{K,E,E'}^m = \int \int_K \mathbf{w}_{K,E}^m \tilde{\mathbf{K}}_K^{-1,m} \mathbf{w}_{K,E'}^m.$$

Similarly, in a fracture gridcell  $k$ , one gets an  $n_k^f \times n_k^f$  SPD matrix  $A_k^f$ , such that:

$$A_k^f = [A_{k,e,e'}^f]_{e,e' \in \partial k}; \quad A_{k,e,e'}^f = \int \int_k \mathbf{w}_{k,e}^f \tilde{\mathbf{K}}_k^{-1,f} \mathbf{w}_{k,e'}^f.$$

The coefficients  $\beta_{K,E}^m$ ,  $\alpha_{K,E}^m$ , and  $\alpha_K^m$  in Eqs. (28) and (20) are defined by:

$$\beta_{K,E,E'}^m = A_{K,E,E'}^{-1,m}; \quad \alpha_{K,E}^m = \sum_{E' \in \partial K} \beta_{K,E,E'}^m; \quad \alpha_K^m = \sum_{E \in \partial K} \alpha_{K,E}^m. \quad (\text{A.1})$$

In the fracture network,  $\alpha_k^f$ ,  $\alpha_{k,e}^f$ , and  $\alpha_e^f$  are defined similarly to those in Eq. (A.1).

The different matrices used to construct the linear system in Eq. (27) are defined in Table A.1, and the matrices appearing in Eq. (27) are given by:

**Table A.1**

Definition of the matrices used to construct the linear system by the MFE method; the symbols  $K$  and  $k$  refer to matrix and fracture gridcells, respectively, and  $E$  and  $e$  refer to matrix–matrix and fracture–fracture interface, respectively

Matrix	Dimensions	Nonzero entries
$D^m$	$N_K^m \times N_K^m$	$D_{K,K}^m = \alpha_K^m$
$\tilde{D}^f$	$N_k^f \times N_k^f$	$\tilde{D}_{k,k}^f = \alpha_k^f$
$M^{m,m}$	$N_E^m \times N_E^m$	$M_{E,E'}^{m,m} = \sum_{K \in \partial E} \beta_{K,E,E'}^m$
$M^{m,f}$	$N_E^m \times N_k^f$	$M_{E,k}^{m,f} = \sum_{K \in \partial E} \beta_{K,E}^m$
$M^{f,f}$	$N_k^f \times N_k^f$	$M_{k,k}^{f,f} = \sum_{e \in \partial k} \beta_{k,e}^f$
$\tilde{M}^f$	$N_k^f \times N_e^f$	$\tilde{M}_{k,e}^f = \sum_{e' \in \partial k} \beta_{k,e,e'}^f$
$\hat{M}^m$	$N_E^m \times N_E^m$	$\hat{M}_{E,E'}^m = \sum_{K \in \partial E} \beta_{K,E,E'}^m$
$\hat{M}^f$	$N_k^f \times N_k^f$	$\hat{M}_{k,k}^f = \sum_{e \in \partial k} \beta_{k,e}^f$
$R^{m,m}$	$N_K^m \times N_K^m$	$R_{K,K}^{m,m} = \alpha_K^m$
$R^{m,f}$	$N_K^m \times N_k^f$	$R_{K,k}^{m,f} = \alpha_{K,E}^m$
$\tilde{R}^f$	$N_k^f \times N_e^f$	$\tilde{R}_{k,e}^f = \alpha_{k,e}^f$
$\hat{R}^m$	$N_K^m \times N_E^m$	$\hat{R}_{K,E}^m = \alpha_{K,E}^m$
$\hat{R}^f$	$N_k^f \times N_e^f$	$\hat{R}_{k,e}^f = \alpha_{k,e}^f$

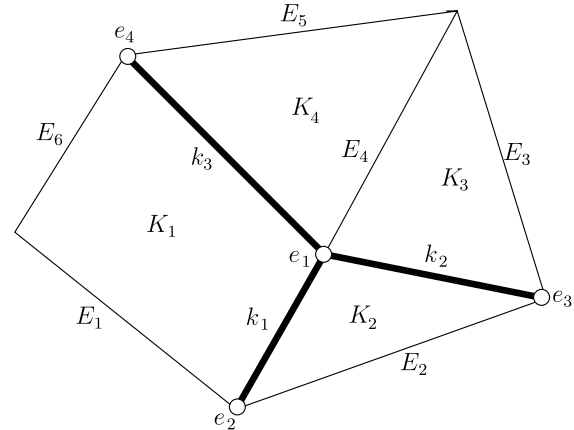


**Fig. B.1.** 2D fractured media with four matrix gridcells and three intersecting fractures.

**Table B.1**

Mesh labels used in Fig. B.1

	Number	Labels
Matrix gridcells	$N_K^m = 4$	$K_1, K_2, K_3, K_4$
Fracture gridcells	$N_k^f = 3$	$k_1, k_2, k_3$
Matrix interfaces	$N_E^m = 6$	$E_1, E_2, E_3, E_4, E_5, E_6$
Fracture interfaces	$N_e^f = 4$	$e_1, e_2, e_3, e_4$

$$\begin{aligned} A^{m,m} &= (M^{m,m} - R^{T,m,m} D^{-1,m} R^{m,m}), \\ A^{m,f} &= (M^{m,f} - R^{T,m,m} D^{-1,m} R^{m,f}), \\ A^{f,m} &= (M^{f,m} - R^{T,m,f} D^{-1,m} R^{m,m}), \\ A^{f,f} &= (M^{f,f} + \tilde{D}^f - R^{T,m,f} D^{-1,m} R^{m,f}). \end{aligned} \quad (\text{A.2})$$

The matrices  $A^{m,m}$  and  $A^{f,f}$  are symmetric and  $A^{m,f} = A^{f,m}$ .

## Appendix B. Structure of the linear system

Consider the 2D fractured media sketched in Fig. B.1. The matrix and fracture gridcells in Fig. B.1 are defined in Table B.1. The linear system in Eq. (27) for the calculation of the wetting-phase potential for the 2D mesh in Fig. B.1 has the following structure.

$$\begin{pmatrix} & E_1 & E_2 & E_3 & E_4 & E_5 & E_6 & k_1 & k_2 & k_3 & e_1 & e_2 & e_3 & e_4 \\ E_1 & \times & 0 & 0 & 0 & 0 & \times & \times & 0 & \times & 0 & 0 & 0 & 0 \\ E_2 & & \times & 0 & 0 & 0 & 0 & \times & \times & 0 & 0 & 0 & 0 & 0 \\ E_3 & & & \times & \times & 0 & 0 & 0 & \times & 0 & 0 & 0 & 0 & 0 \\ E_4 & & & & \times & \times & 0 & 0 & \times & \times & 0 & 0 & 0 & 0 \\ E_5 & & & & & \times & 0 & 0 & 0 & \times & 0 & 0 & 0 & 0 \\ E_6 & & & & & & \times & \times & 0 & \times & 0 & 0 & 0 & 0 \\ k_1 & & & & & & & \times & \times & \times & \times & \times & 0 & 0 \\ k_2 & & & & & & & & \times & 0 & \times & 0 & \times & 0 \\ k_3 & & & & & & & & & \times & \times & 0 & 0 & \times \\ e_1 & & & & & & & & & & \times & \times & \times & \times \\ e_2 & & & & & & & & & & & \times & 0 & 0 \\ e_3 & & & & & & & & & & & & \times & 0 \\ e_4 & & & & & & & & & & & & & \times \end{pmatrix}$$

## References

- [1] Barenblatt G, Zheltov Y, Kochina I. Basic concepts in the theory of seepage of homogeneous fluids in fissurized rocks. J Appl Math Mech 1983;24(5):1286–303.
- [2] Warren J, Root P. The behavior of naturally fractured reservoirs. SPE J 1963;245–55.

- [3] Kazemi H, Gilman J. Pressure transient analysis of naturally fractured reservoirs with uniform fracture distribution. *SPE J* 1969(December):451–62.
- [4] Thomas L, Dixon T, Pierson R. Fractured reservoir simulation. *SPE J* 1983;42–54.
- [5] Kazemi H, Gilman J. Analytical and numerical solution of oil recovery from fractured reservoirs with empirical transfer functions. *SPE J* 1992(May):219–27.
- [6] Kazemi H, Merrill L. Numerical simulation of water imbibition in fractured cores. *SPE J* 1979(June):175–82.
- [7] Pruess K, Narasimhan T. A practical method for modeling fluid and heat flow in fractured porous media. *SPE J* 1985;25(1):14–26.
- [8] Ghorayeb K, Firoozabadi A. Numerical study of natural convection and diffusion in fractured porous media. *SPE J* 2000;5(1):12–20.
- [9] Noorishad J, Mehran M. An upstream finite element method for solution of transient transport equation in fractured porous media. *Water Resour Res* 1982;18(3):588–96.
- [10] Baca R, Arnett R, Langford D. Modeling fluid flow in fractured porous rock masses by finite element techniques. *Int J Num Meth Fluids* 1984;4:337–48.
- [11] Lee S, Jensen C, Lough M. Efficient finite-difference model for flow in a reservoir with multiple length-scale fractures. *SPE J* 2000;5(3):268–75.
- [12] Yortsos Y, Chang J. Capillary effects in steady-state flow in heterogeneous cores. *Transport Porous Med* 1990;5(4):399–420.
- [13] Van Duijn C, Molenaar J, De Neef M. The effect of capillary forces on immiscible two-phase flow in heterogeneous porous media. *Transport Porous Med* 1995;21(1):71–93.
- [14] Van Duijn C, De Neef M. Similarity solution for capillary redistribution of two phases in a porous medium with a single discontinuity. *Adv Water Res* 1998;21(6):451–61.
- [15] Correa A, Firoozabadi A. Concept of gravity drainage in layered porous media. *SPE J* 1996(March):101–11.
- [16] Slough K, Sudicky E, Forsyth P. Grid refinement for modeling multiphase flow in discretely fractured porous media. *Adv Water Res* 1999;23:261–9.
- [17] Slough K, Sudicky E, Forsyth P. Numerical simulation of multiphase flow and phase partitioning in discretely fractured geologic media. *J Contam Hydrol* 1999;40:107–36.
- [18] Granet S, Fabrie P, Lemmonier P, Quitard M. A single phase flow simulation of fractured reservoir using a discrete representation of fractures. In: *Proceedings of the 6th European conference on the mathematics of oil recovery (ECMOR VI)*, September 8–11, Peebles, Scotland, UK; 1998.
- [19] Juanes R, Samper J, Molinero J. A general and efficient formulation of fractures and boundary conditions in the finite element method. *Int J Numer Meth Eng* 2002;45:1751–74.
- [20] Zhang K, Woodbury A. A krylov finite-element approach for multi-species contaminant transport in discretely fractured porous media. *Adv Water Res* 2002;25:705–21.
- [21] Kim J, Deo M. Comparison of the performance of a discrete fracture multiphase model with those using conventional methods. In: *Reservoir simulation symposium*, 14–17 February, Houston, TX; 1999. No. SPE51928.
- [22] Kim J, Deo M. Finite element discrete fracture model for multiphase flow in porous media. *AIChE J* 2000;46(6):1120–30.
- [23] Karimi-Fard M, Firoozabadi A. Numerical simulation of water injection in 2D fractured media using discrete-fracture model. *SPERE J* 2003;4(March):117–26.
- [24] Karimi-Fard M, Durlinsky L, Aziz K. An efficient discrete-fracture model applicable for general-purpose reservoir simulators. *SPE J* 2004;9(2):227–36.
- [25] Granet S, Fabrie P, Lemmonier P, Quitard M. A two-phase flow simulation of a fractures reservoir using a new fissure element method. *J Petrol Sci Eng* 2001;32(1):35–52.
- [26] Bastian P, Helmig R. Efficient fully-coupled solution techniques for two-phase flow in porous media. parallel multigrid solution and large scale computations. *Adv Water Res* 1999;23:199–216.
- [27] Bastian P, Helmig R, Jakobs H, Reichenberger V. Numerical simulation of multiphase flow in fractured porous media. In: *Numerical treatment of multiphase flows in porous media*. In: Chen, Ewing, Shi, editors. *Lecture notes in physics*, vol. 552. Springer-Verlag; 2000. p. 1–18.
- [28] Bogdanov I, Mourzenko V, Thovert J, Adler P. Two-phase flow through fractured porous media. *Phys Rev E* 2003;68(2):1–24.
- [29] Monteagudo J, Firoozabadi A. Control-volume method for numerical simulation of two-phase immiscible flow in two- and three-dimensional discrete-fractured media. *Water Resour Res* 2004;40(7):W07405.
- [30] Geiger S, Roberts S, Matthäi S, Zoppou C, Burri A. Combining finite element and finite volume methods for efficient multiphase flow simulations in highly heterogeneous and structurally complex geologic media. *GeoFluids* 2004;4(4):284–99.
- [31] Matthäi S, Mezentsev A, Belayneh M. Control-volume finite-element two-phase flow experiments with fractured rock represented by unstructured 3D hybrid meshes. In: *Reservoir simulation symposium*, 31 January–2 February, The Woodlands, TX; 2005.
- [32] Monteagudo J, Firoozabadi A. Control-volume model for simulation of water injection in fractured media: Incorporating matrix heterogeneity and reservoir wettability effects. *SPE J* 2007;12(3):355–66.
- [33] Reichenberger V, Jakobs H, Bastian P, Helmig R. A mixed-dimensional finite volume method for two-phase flow in fractured porous media. *Adv Water Res* 2006;29:1020–36.
- [34] Hoteit H, Firoozabadi A. Numerical modeling of diffusion in fractured media for gas injection and recycling schemes. In: *Annual technical conference and exhibition*, 4–27 September, San Antonio, TX; 2006. No. SPE103292.
- [35] Raviart P, Thomas J. A mixed hybrid finite element method for the second order elliptic problem. *Lectures notes in mathematics*, vol. 606. New York: Springer-Verlag; 1977.
- [36] Brezzi F, Fortin M. Mixed and hybrid finite element methods. *Environmental engineering*. New York: Springer-Verlag; 1991.
- [37] Maryška J, Severýn O, Vohralík M. Numerical simulation of fracture flow with a mixed-hybrid FEM stochastic discrete fracture network model. *Comput Geosci* 2003;8(3):1499–573.
- [38] Vohralík M, Maryška J, Severýn O. Mixed and nonconforming finite element methods on a system of polygons. *Appl Numer Math* 2007;57:176–93.
- [39] Alboin C, Jaffré J, Roberts J, Serres C. Modeling fractures as interfaces for flow and transport in porous media. In: *Chen, Ewing, editors. Fluid flow and transport in porous media*, vol. 295. American Mathematical Society; 2002. p. 13–24.
- [40] Martin V, Jaffré J, Roberts J. Modeling fractures and barriers as interfaces for flow in porous media. *SIAM* 2005;26:1667–91.
- [41] Chavent G, Roberts J. A unified physical presentation of mixed, mixed-hybrid finite element method and standard finite difference approximations for the determination of velocities in water flow problems. *Adv Water Res* 1991;14(6):329–33.
- [42] Chavent G, Jaffré J. Mathematical models and finite elements for reservoir simulation. *Studies in mathematics and its applications*. North-Holland: Elsevier; 1986.
- [43] Hoteit H, Firoozabadi A. Numerical modeling of two-phase flow in heterogeneous permeable media with different capillarity pressures. *Adv Water Res* 2008;31:56–73.
- [44] Coats K. An equation of state compositional model. *SPE J* 1980:363–76.
- [45] Hoteit H, Firoozabadi A. Compositional modeling by the combined discontinuous Galerkin and mixed methods. *SPE J* 2006;11(1):19–34.
- [46] Cockburn B, Shu C. TVB Runge–Kutta local projection discontinuous Galerkin finite element method for conservative laws II: general frame-work. *Math Comp* 1989;52:411–35.
- [47] Cockburn B, Shu C. The Runge–Kutta discontinuous Galerkin method for conservative laws V: multidimensional systems. *J Comput Phys* 1998;141:199–224.
- [48] Monteagudo J, Firoozabadi A. Comparison of fully-implicit and IMPES formulations for simulation of water injection in fractured and unfractured media. *Inter J Numer Meth Eng* 2006;69(4):698–728.
- [49] Thomas J. Sur l'analyse numérique des méthodes d'élément finis hybrides et mixtes. Ph.D. thesis, Univ. de Pierre et Marie Curie, France; 1977.
- [50] Hoteit H, Erhel J, Mosé R, Bernard P, Ackerer P. Numerical reliability for mixed methods applied to flow problems in porous media. *Comput Geosci* 2002;6(2):161–94.
- [51] Hoteit H, Firoozabadi A. Compositional modeling by the combined discontinuous Galerkin and mixed methods. *SPE J* 2006;11(1):19–34.
- [52] Hoteit H, Firoozabadi A. Compositional modeling of discrete-fractured media without transfer functions by the discontinuous Galerkin and mixed methods. *SPE J* 2006;11(3):341–52.
- [53] Hoteit H, Firoozabadi A. Multicomponent fluid flow by discontinuous Galerkin and mixed methods in unfractured and fractured media. *Water Resour Res* 2005;41(11):W11412.